ELSEVIER

Progress in Surface Science 74 (2003) 251–268

Progress in SURFACE SCIENCE

www.elsevier.com/locate/progsurf

Enhanced electron–phonon coupling at metal surfaces

E.W. Plummer [a,b,*], Junren Shi [b], S.-J. Tang [a], Eli Rotenberg [c], S.D. Kevan [d]

[a] *Department of Physics and Astronomy, The University of Tennessee, Knoxville, TN 37996, USA*
[b] *Condensed Matter Sciences Division, Oak Ridge National Laboratory, Oak Ridge, TN 37831, USA*
[c] *Advanced Light Source, Lawrence Berkeley National Laboratory, Berkeley, CA 947720, USA*
[d] *Department of Physics, University of Oregon, Eugene, OR 97403, USA*

Abstract

Recent advances in experimental techniques and theoretical capabilities associated with the study of surfaces show promise for producing in unprecedented detail a picture of electron–phonon coupling. These investigations on surfaces of relatively simple metals can be the platform for understanding functionality in complex materials associated with the coupling between charge and the lattice. In this article, we present an introduction to electron–phonon coupling, especially in systems with reduced dimensionality, and the recent experimental and theoretical achievements. Then, we try to anticipate the exciting future created by advances in surface physics.

Keywords: Electron–phonon coupling; Eliashberg function; Surface states; Angle-resolved photoemission; Self-energy; Kohn anomaly; Fermi contours; Helium atom scattering; Inelastic electron scattering

1. Introduction

Electron–phonon interaction in metals is a very old subject. Göran Grimvall in the preface to his classic book on this subject pointed out that 1000 papers had been published in this subject field between 1960 and 1980 [1]. What can be new and exciting in such an old and mature field? The answer is *surfaces and surface science*

* Corresponding author. Address: Department of Physics and Astronomy, The University of Tennessee, Knoxville, TN 37996-1501, USA. Tel.: +1-423-974-0768; fax: +1-423-974-6378.
E-mail address: eplummer@utk.edu (E.W. Plummer).

0079-6816/$ - see front matter
doi:10.1016/j.progsurf.2003.08.033

techniques. Recent advances in experimental techniques coupled with ever-growing theoretical capabilities promise to create a renaissance in this subject. High-resolution angular-resolved photoemission is producing direct images of the distortion of the two-dimensional surface state bands near the Fermi energy because of electron–phonon coupling (EPC) [2–6]. First-principles calculations of the EPC for surface states are appearing in the literature [7–9] which not only explain the origin of the EPC-induced band distortions but also produce exquisite pictures of the Eliashberg function $\alpha^2F(\omega)$ [1]. The Eliashberg function is the product of a coupling constant times the phonon density of states and is at the heart of any theory of EPC [1]. A recent theoretical advance that will be described in this paper will allow experimentalists to extract the Eliashberg function directly from the high-resolution photoemission data [6]. These developments mark the beginning of a new era or a renaissance in the elucidation of many-body effects in reduced dimensionality.

Before continuing, it is important to back up and describe exactly what is implied by the Born-Oppenheimer approximation or the adiabatic approximation because EPC is a breakdown of the adiabatic approximation [1]. The total Hamiltonian for electrons and ions contains terms for the kinetic energy of the electrons and ions as well as the e–e and ion–ion Coulomb potential energy. The potential energy $U_{\text{ion–e}}(\boldsymbol{r}_i, \boldsymbol{R}_j)$ between the ZN electrons located at $\boldsymbol{r}_i$ and the N ions located at $\boldsymbol{R}_j$ couples the ions and the electrons. In principle, we would like to find the solution for the Schrödinger equation ψ_{tot} for this Hamiltonian, but it is impossible, and assumptions have to be made. The first assumption is that ψ_{tot} can be written as a product of two wave functions

$$\psi_{\text{tot}}(\boldsymbol{r}_i\boldsymbol{R}_j) = \psi_{\text{e}}(\boldsymbol{r}_i, \boldsymbol{R}_j)\psi_{\text{ion}}(\boldsymbol{R}_j). \tag{1}$$

The second assumption is the adiabatic approximation where it is assumed that since the ions move so slowly compared with the electrons that the electrons follow their motion adiabatically. In an adiabatic motion, an electron does not make transitions from one state to another; instead, the electronic state $\psi_{\text{e}}(\boldsymbol{r}_i, \boldsymbol{R}_j)$ is the ground state for any configuration of the ions. At $T = 0$, the ground state of the electronic system can be calculated with the equilibrium positions of the ions. This static lattice configuration is what will be used for the dispersion of the two-dimensional surface states, $\varepsilon_0(\mathbf{k})$, in the absence of any EPC.

Now, it is clear what must be considered in the nonadiabatic regime necessary to explain EPC—the coupling of the excitation spectra of the electrons and the lattice. The static electronic band structure represented by $\varepsilon_0(\mathbf{k})$ will be distorted by coupling to the phonon modes of the lattice. The screening of the electrons by the lattice is represented by the self-energy function $\Sigma(\mathbf{k}, E)$ where the quasi-particle band dispersion with EPC will be given by

$$\varepsilon(\mathbf{k}) = \varepsilon_0(\mathbf{k}) + \text{Re}\Sigma(\mathbf{k}, E). \tag{2}$$

The imaginary part of the self-energy is related to the lifetime τ of the excited electronic states,

$$\tau^{-1} = 2\,\text{Im}\Sigma(\mathbf{k}, ET). \tag{3}$$

In this case, the temperature dependence of the self-energy will give the temperature-dependent linewidth.

A simple representation for the two independent systems is shown in Fig. 1 where (a) is the electron dispersion for a simple free-electron metal showing the Fermi energy (E_F) and Fermi wave vector (k_F) and (b) shows the phonon dispersion for a monatomic lattice. It is clear from the previous discussion that what is required when the systems are coupled is the excitation spectrum. For EPC to be important, the spectrum of electronic excitations must be degenerate, or nearly so, with the elementary lattice excitation (phonons) in the system [Fig. 1(b)]. Metals, by definition, satisfy this condition because there are always low-energy excitations at the Fermi energy. Fig. 2 shows the allowed excitation energy as a function of the momentum transfer for (a) a one-dimensional metal and (b) a higher dimensional metal. Fig. 1(b) is the lattice excitation spectra as a function of momentum. It is essential to

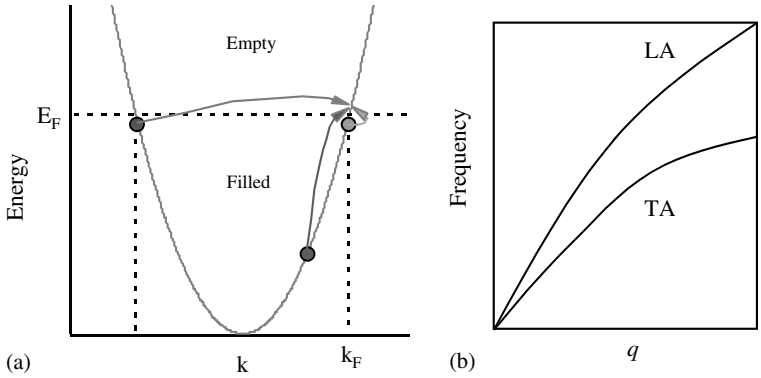

Fig. 1. (a) A simple free electron band structure showing the possible transitions creating electron–hole pairs. (b) Phonon dispersion for a monatomic metal in one direction showing the longitudinal and transverse acoustic modes.

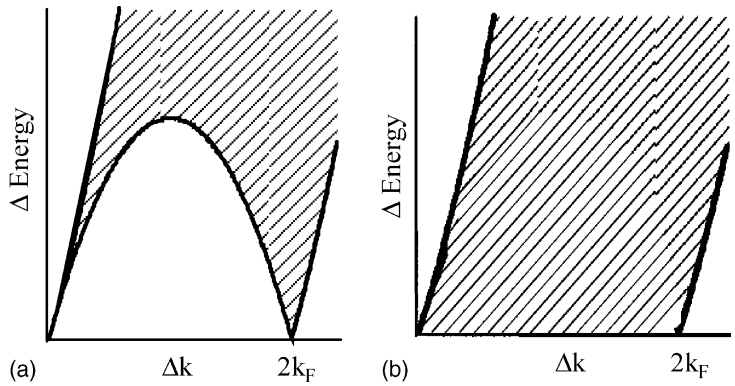

Fig. 2. The electron–hole pair excitation spectrum derived from the free electron band structure shown in Fig. 1(a). (a) For a one-dimensional system and (b) for a two-dimensional system.

understand the scale in these two figures. The temperature of the Fermi energy electron in Al is 10^5 K, while the Debye temperature of the lattice vibrations is only 394 K. Therefore, the distortion of the electronic bands due to EPC will occur only within a narrow energy window around the Fermi energy [see Fig. 3(a)] defined by the maximum energy in the phonon density of states. This statement is not true for the EPC contribution to the linewidth (Eq. (3)). Excitations from deep in the band will display a temperature-dependent linewidth because EPC is involved in the decay process [6,10–17].

Fig. 3(a) displays the distortion to the electronic band dispersion near the Fermi energy anticipated from EPC. It is easy to see that one consequence is that the EPC causes a mass enhancement in the electronic band at the Fermi energy. The mass enhancement factor λ is defined by [1]

$$\lambda = (m^* - m_0)/m_0 \tag{4}$$

where m^* is the electron effective mass at the Fermi energy and m_0 is the effective mass in a frozen lattice, i.e., without EPC. If the low-energy lattice excitations (phonons) distort the electronic bands, then the low-energy electronic excitation close to the Fermi energy should distort the phonon dispersion curves shown in Fig. 1(b). In 1959, Kohn pointed out that the $2k_F$ excitations shown in Fig. 1(a) could lead, via the screened ion–ion interaction, to a dip in the phonon dispersion curves at this value of q [19]. These dips are represented in Fig. 3(b) and are known as *Kohn anomalies*.

A Kohn anomaly occurs in the phonon dispersion curves when there is a single vector connecting extremal sections of the Fermi surface (nesting). Two sections of the Fermi surface need to be parallel over some extended range in k-space. This is much easier to achieve as the dimensionality is reduced. Saturated H adsorption on

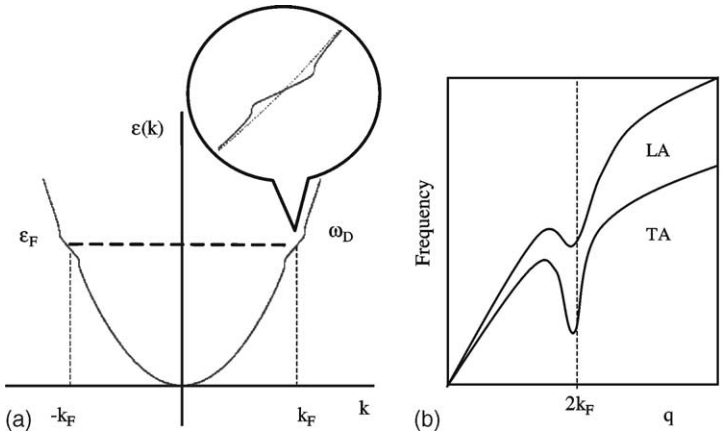

Fig. 3. An illustration of the effects of electron–phonon coupling. (a) EPC causes a distortion in the band dispersions near the Fermi energy. (b) Electron–hole pair excitations across the Fermi surface [see Fig. 1(a)] can lead to Kohn anomalies or dips in the phonon dispersion at $q = 2k_F$ [19].

W(1 1 0) or Mo(1 1 0) is probably the best known and studied example of Kohn anomalies and Fermi surface nesting at surfaces [5,15,20–24] and will be described subsequently. In one-dimension, a monatomic chain is unstable because of Fermi surface nesting. Figs. 1(a) and 2(b) show that there is one and only one vector that connects two points on the Fermi surface, i.e., perfect nesting. This leads to a singularity in the one-dimensional Lindhard response function [25] and "giant Kohn anomalies" in the phonon dispersion at $2k_F$. In the one-dimensional system, k_F is one half of the zone boundary at π/a (a lattice spacing); therefore the giant Kohn anomaly occurs at the zone boundary. If the phonon frequency at $2k_F = \pi/a$ goes imaginary, the monatomic chain will reconstruct. The new periodicity will be $2\pi/q$ (soft phonon) $= 2\pi/2k_F = 2\pi/(\pi a) = 2a$. The pairing of the atoms creates a new unit cell with the zone boundary at $\pi/2a$, a gap in the electronic states at the Fermi energy (metal–insulator transition), and an optical phonon branch. Dimensionality of the system is important when discussing EPC.

As promised, the H/W(1 1 0) system will now be described. It offers a beautiful example of all the concepts discussed above. Adsorption of H onto a clean W(1 1 0) surface shifts the surface states continuously [20], and at saturation, a Kohn anomaly is observed in the surface phonon dispersion using He atom scattering (HAS) [21]. The HAS data in Fig. 4(a) show a very deep dip in the phonon energy at $q = 0.93$ Å^{-1}. This has to be the signature of $2k_F$ Fermi surface nesting, but the early photoemission Fermi contour measurements for the hydrogen-covered surface did not show this nesting vector [20]. Subsequent calculations of the Fermi contours showed segments that were appropriately nested [22]. These calculated surface states [22] are shown on the plot of the Fermi contours in Fig. 4(b). This surface state, labeled 1, is connected by a spanning vector of magnitude 0.96, in close agreement with the experimental value. The calculated phonon dispersion is shown as the solid lines in Fig. 4(a), displaying dips, but not as large as seen with HAS [23]. On the other hand, inelastic electron scattering data (EELS) [24] shown in Fig. 4(a) are almost identical to the calculations. There are two explanations in the literature for the discrepancy between the HAS and EELS data. The first, and obviously the one most compatible with EPC, is that in this region of energy and momentum there is mixing between the excitations of the electrons and the lattice [22]. The deep dip seen by HAS is primarily electronic in origin due to Fermi surface nesting, while the shallow branch seen by ELS is primarily lattice vibrations [22]. The second explanation [23] is that at saturation coverage the hydrogen forms a disordered layer and the mode is a collective plasmonlike mode associated with the diffusive motion.

The recent photoemission measurements of the Fermi contours for this system displayed in Fig. 4(b) expand upon these results in an important and interesting way—enhanced spin-orbit coupling at a surface [5,15,26]. The spin-orbit interaction is enhanced because of the broken symmetry at the surface [27]. The Fermi contour implicated in the calculations as being responsible for the anomaly was found to be significantly split into two bands, labeled 1 and 2 in this figure. The two states are observed to be 100% spin polarized and to support an unusual spin structure in k-space [26]. The observed phonon anomaly is now understood to be associated with nesting between contours 1 and 2, which are coupled by a vector of magnitude 0.87

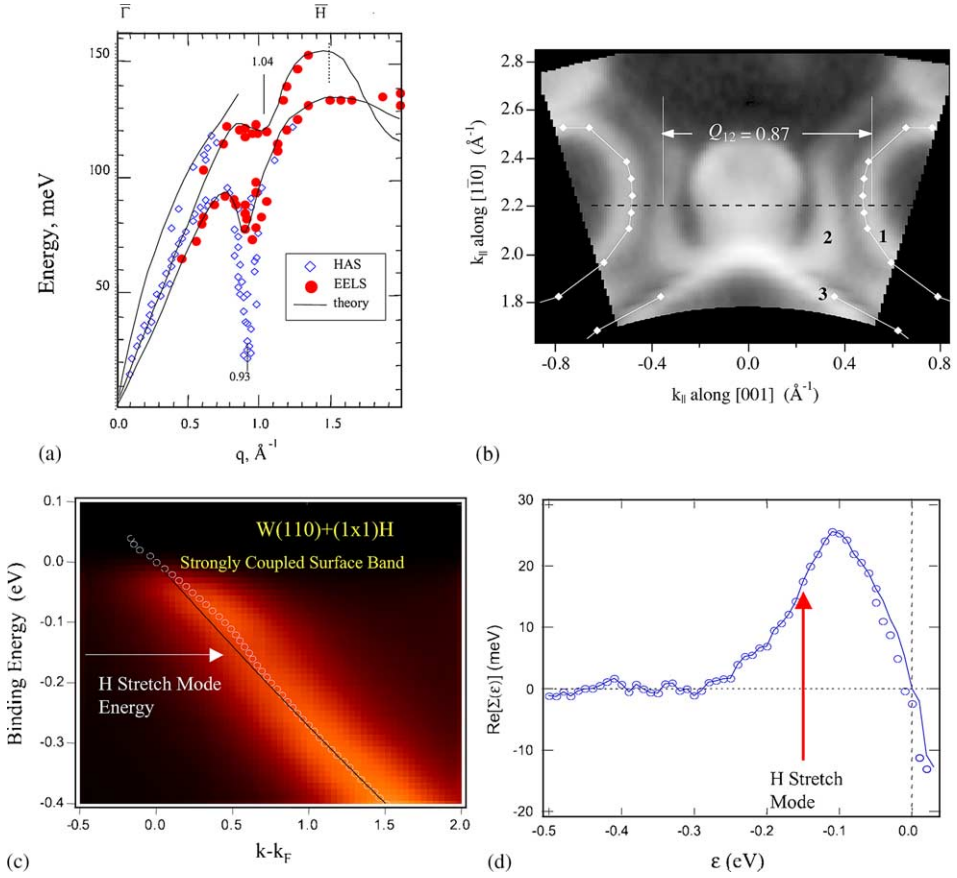

Fig. 4. Illustration of the effects of EPC for saturated H adsorption on W(1 1 0). (a) Display of the measured (HAS Ref. [21] and EELS Ref. [24]) and calculated phonon dispersion [23] in the Σ direction of the SBZ. (b) Measurements of the Fermi contour by a photoemission display system [5,15]. The Fermi contour of the calculated surface states #1 and #3 are shown [22] as well as the experimentally determined nesting vector between the spin-orbit split surface states #1 and #3 [26]. (c) Photoemission display of surface state #1 dispersion near the Fermi energy [5,15] with an arrow marking the energy of the H stretch mode at 161 meV [24]. (d) $\mathrm{Re}\Sigma(\varepsilon)$ determined from the data shown in (c).

$\mathring{\mathrm{A}}^{-1}$. As shown in this figure, nesting between each individual contour and its image opposite the $\overline{\Sigma}$ line does not match the position of the observed anomaly as well. Moreover, the initially proposed [5] and recently measured [26] spin structure does not allow coupling between each contour and its image because these states have opposite spin, and the electron-phonon interaction is spin-independent. In this simple surface system, we find all the ingredients of strong coupling between spin, charge, and lattice degrees of freedom.

How strong are these couplings? An indication is offered in Fig. 4(c), which displays the surface state 1 dispersion revealing the distortion due to EPC near the Fermi energy, and by Fig. 4(d), which shows $\mathrm{Re}\Sigma(\varepsilon)$ extracted from these data [15].

The authors measured a mass enhancement factor of $\lambda = 1.4$ for surface state #1 near the Fermi energy—an anomalously high value indicative of strong coupling indeed. Moreover, they assigned the coupling to the high-energy (161-meV) hydrogen symmetric stretching mode, and the energy-coupling parameter pair is notably anomalous [24]. Even though this system has been studied for many years and both the data and theory are consistent, there are still important unresolved questions, especially pertaining to the origin of the EPC. The EPC, as displayed by the $\mathrm{Re}\Sigma$ in Fig. 4(d), cannot be explained with any simple phonon model, and it is clear from looking at these data and the arrow showing the position of the H stretching mode that the eventual answer will be more complicated than having a single vibrational mode coupling to the electrons [5,15].

Before leaving this section, it is important to talk briefly about line shapes and linewidths. Fig. 5(a) displays the temperature dependence of the photoemission linewidth from the bottom of the Be(0 0 0 1) surface state (2.78-eV binding energy) [12]. The increase in width as the temperature is increased is a consequence of the temperature dependence in $\mathrm{Im}\Sigma(T)$ expressed in Eq. (3). The high-temperature limit gives the following equation [12]

$$\mathrm{d}\Delta E/\mathrm{d}T = 2\pi\lambda k_{\mathrm{B}}, \tag{5}$$

where λ is the mass enhancement factor given in Eq. (4) and $\Delta E(T)$ is the width of the peaks in the photoemission spectra. Using this equation, the data shown in Fig. 5(a) yield a value of $\lambda = 1.06$ [11]. The H and D vibrational modes [shown in Fig. 5(b)] are measured using infrared spectroscopy [28], exhibiting another fundamental line shape effect due to EPC. The H–W mode at 1270 cm^{-1} is assigned to the overtone of

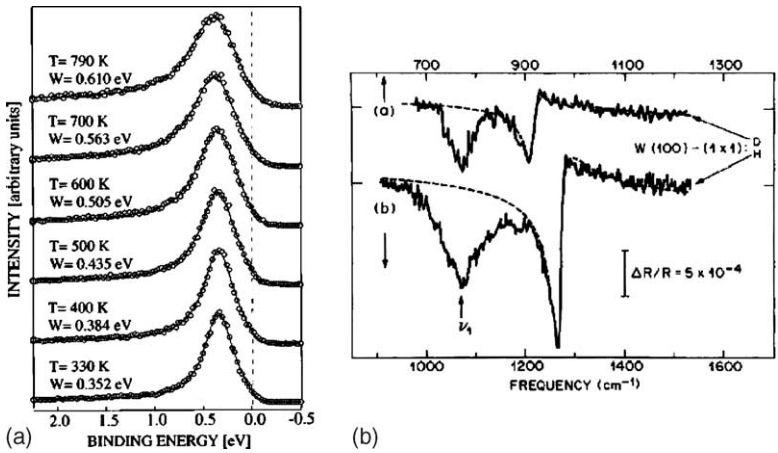

Fig. 5. Illustration of the effect of EPC on the linewidths and line shapes. (a) Temperature dependence of the angle-resolved photoemission spectra from the bottom of the surface state band on Be(0 0 0 1) [12]. (b) Infrared spectra of H adsorbed on W(1 0 0) showing the Fano line shape for the overtone of the wagging mode for both H and D [28].

the wagging-mode. The Fano line shape is a direct result of the EPC of this mode to the continuum of electronic excitations [29].

2. Present status of EPC measurements and calculations for surfaces

Before describing the present status of measurements of the EPC at metal surfaces, it is useful to briefly summarize the important theoretical procedure for calculating the distortion of the electronic bands near the Fermi energy and the line shape as seen in a photoemission spectrum. This requires calculating the self-energy $\Sigma(\varepsilon, \boldsymbol{k}, T)$. At the heart of any calculation or representation of the EPC is the Eliashberg function $E(\omega, \varepsilon, \mathbf{k}) = \alpha^2(\omega, \mathbf{k})F(\omega, \varepsilon, \mathbf{k})$, where ω is the phonon energy, ε is the electron energy, and $\mathbf{k}$ is the wave vector of the electronic state. In general, the electronic bandwidth is large compared with the phonon bandwidth where the ε dependence is negligible. Here we will also ignore the $\mathbf{k}$ dependence. Then, $E(\omega) = \alpha^2(\omega)F(\omega)$, which is usually written as $E(\omega) = \alpha^2 F(\omega)$. With this formulation, the $\mathrm{Re}\Sigma(\varepsilon, T)$ is written as

$$\mathrm{Re}\Sigma(\varepsilon, T) = \int_0^\infty \mathrm{d}\omega' G\left(\frac{\varepsilon}{kT}, \frac{h\omega'}{kT}\right) E(\omega') \tag{6}$$

with the function G given by

$$G(y, y') = \int_{-\infty}^{\infty} \mathrm{d}x \frac{2y'}{x^2 - y'^2} f(x + y). \tag{7}$$

The Fermi distribution function is represented by $f(x)$. The form of the $\mathrm{Re}\Sigma$ for a simple Debye model of the phonon density of states is illustrated in Fig. 6(a). In this case, the Eliashberg function is simply given by $\lambda(\omega/\omega_\mathrm{D})^2$ for $\omega < \omega_\mathrm{D}$ and zero for larger ω. Because the Eliashberg function is zero above the top of the phonon band, the $\mathrm{Re}\Sigma$ peaks near the maximum phonon energy ω_D.

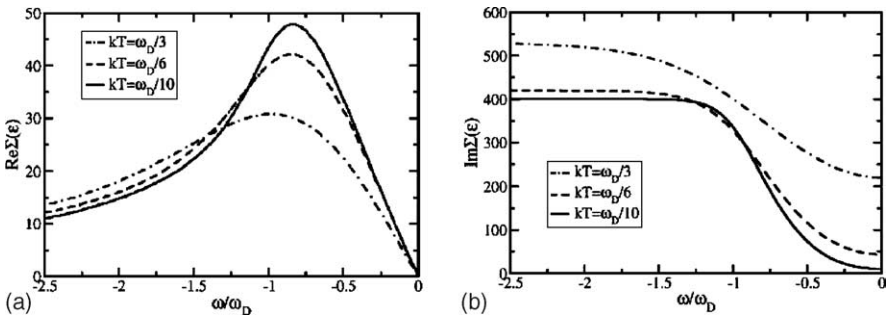

Fig. 6. Calculated behavior of the EPC self-energy $\Sigma(\varepsilon, \mathbf{k}, T)$ using a simple Debye model for the phonon density of states. (a) $\mathrm{Re}\Sigma(\varepsilon, T)$ for several temperatures with respect to the Debye energy ω_D. The energy scale is normalized to the Debye energy ω_D. (b) The $\mathrm{Im}\Sigma(\varepsilon, T)$ for the same temperatures used in (a).

The technique commonly used to determine the mass enhancement factor λ is to calculate the slope of the $\mathrm{Re}\Sigma$ at the Fermi energy

$$\lambda = -\mathrm{dRe}\Sigma(\varepsilon_\mathrm{F})/\mathrm{d}\varepsilon \tag{8}$$

One of the major problems with this procedure is shown in Fig. 6(a)—the $\mathrm{Re}\Sigma(\varepsilon, T)$ is temperature-dependent. There is a 30% reduction in $-\mathrm{de}\Sigma(\varepsilon)/\mathrm{d}\varepsilon$ when the temperature is 1/3 of the Debye temperature. The Eliashberg function is not temperature-dependent, and therefore λ calculated from this function using the following defining equation is not temperature-dependent [1,6]

$$\lambda = 2\int_0^\infty \frac{\mathrm{d}\omega}{\omega}\alpha^2F(\omega) \tag{9}$$

The $\mathrm{Im}s\Sigma(\varepsilon, T)$ is defined by the following equation

$$\mathrm{Im}\Sigma(\varepsilon, \mathbf{k}; kT) = \pi\int_0^\infty \mathrm{d}\omega\alpha^2F(\omega; \varepsilon, \mathbf{k})[1 - f(\varepsilon - \omega) + f(\varepsilon + \omega) + 2n(\omega)], \tag{10}$$

where f and n are the Fermi and Bose distribution functions, respectively. This function is displayed in Fig. 6(b) as a function of temperature and electron energy for the Debye model described above. At $T = 0$, the linewidth will be zero at the Fermi energy and increase monotonically up to a maximum value at $\omega = \omega_\mathrm{D}$. As the temperature increases, the linewidth, or $\mathrm{Im}\Sigma$, increases for all values of ω. It is the temperature dependence of the $\mathrm{Im}\Sigma$ that has been used to extract the mass enhancement factor λ for electronic states with energies much larger than the phonon bandwidth (ω_D) [10–18].

The Eliashberg function [1] is a product of the phonon density of states weighted by the e–p interaction. It represents the probability of emitting a phonon of energy ω at $T = 0$

$$\alpha^2F_i(\omega; \varepsilon, \mathbf{k}) = \int \frac{\mathrm{d}\mathbf{k}}{\Omega_\mathrm{BZ}} \frac{\delta(\varepsilon - \varepsilon_i(\mathbf{k}))}{N_i(\varepsilon)} \int \frac{\mathrm{d}\mathbf{q}}{\Omega_\mathrm{BZ}} \sum_{v,f} |g^{i\to f,v}_{\mathbf{k},\mathbf{k}+\mathbf{q}}|^2 \delta(\varepsilon - \varepsilon_f(\mathbf{k}))\delta(\omega - \omega^v_\mathbf{q}) \tag{11}$$

where

$$g^{i\to f,v}_{\mathbf{k},\mathbf{k}+\mathbf{q}} = \langle \Psi_{i,\mathbf{k}} | \Delta V^v_\mathbf{q} | \Psi_{f,\mathbf{k}+\mathbf{q}} \rangle \tag{12}$$

is the e–p matrix element calculated using the electronic state wave functions ψ and the self-consistent electron potential induced by the phonon mode with momentum $\mathbf{q}$ and mode index v [1,7,8]. The index of the surface state is i, the final state index is f, and the binding energy of the electronic state is ε. Ω_BZ is the area of the 2D surface Brillouin zone (SBZ).

The present experimental and theoretical capabilities can be illustrated using one system, Be(0 0 0 1) [3,4,8,12]. The location of the surface states in this system is shown in Fig. 7. The surface state that has been studied the most is the one at the SBZ center. It has a binding energy of 2.78 eV at the zone center, crosses the Fermi energy at $k_\mathrm{F} = 0.95$ A^{-1} (effective mass of 1.17), and has an almost circular Fermi

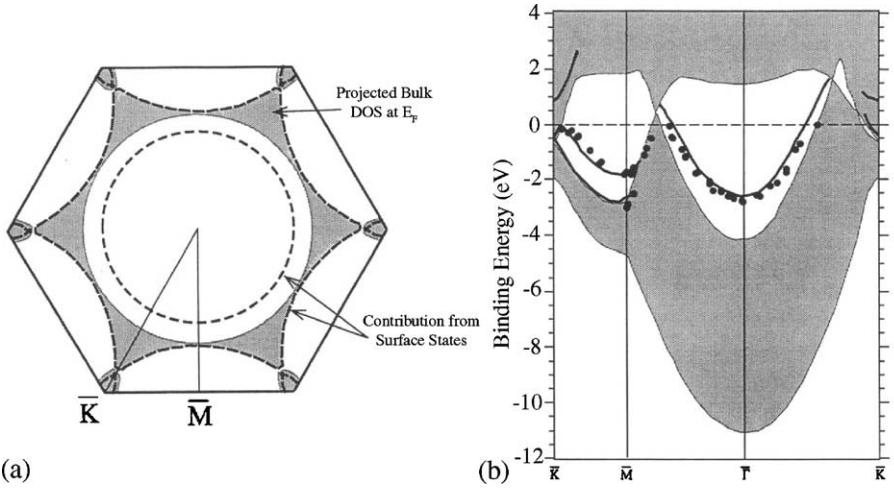

Fig. 7. Electronic properties of the Be(0 0 0 1) surface. (a) The projection of the bulk bands (shaded) onto the SBZ. The dashed lines are the surface states [30,31]. (b) The projection of the bulk bands (shaded) along the high-symmetry directions of the SBZ. The solid lines and data are for the surface states [32].

contour [12]. The temperature dependence of the photoemission linewidth for the surface state at the SBZ center is displayed in Fig. 5(a) [12]. Fig. 8 shows the analysis of these data [12]. If the authors used the high-temperature limit expressed in Eq. (5), they obtained $\lambda = 1.06$. The problem is that the Debye temperature of bulk Be is 1000 K, and these data are for temperatures appreciably lower. In an attempt to overcome this difficulty, the authors assumed that the Eliashberg function in Eq. (11) could be modeled by a 3D Debye model with the maximum frequency dictated by the Debye temperature of the bulk. This fit is shown in Fig. 8 by the dashed line, yielding $\lambda = 1.25$. In a later paper, LaShell et al. [4] pointed out that the analysis in

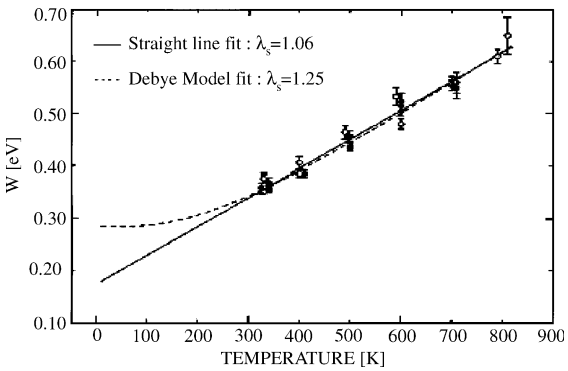

Fig. 8. A plot of the surface-state widths from the fit to the data shown in Fig. 5(a) [12]. The error bars on the data are statistical uncertainties from the fits. The open circles are for increasing temperatures and the filled circles are for decreasing temperatures [12].

the first paper [12] was incorrect because of the effect of the finite acceptance angle and the curvature of the bands. They estimated that the correction factor was 1.32, yielding a new $\lambda = 0.87$ [4].

The EPC band distortion near the Fermi energy has also been utilized to extract a value of λ for this surface state [3,4]. Fig. 9 exhibits the data of LaShell et al. [4] taken at 40 K. Panel (c) shows the $\mathrm{Re}\Sigma(\varepsilon)$ at the bottom and the $\mathrm{Im}\Sigma$ at the top. The slope of $\mathrm{Re}\Sigma(\varepsilon_F)$ at the Fermi energy was 0.7 ± 0.1. The solid lines are the best fit using a Debye model for the Eliashberg function. It is easy to see that this model does not fit the data very well; therefore, the value of $\lambda = 0.65$ obtained from this fitting procedure is probably not very dependable. The optimal value of ω_D was 65 meV, appreciably lower than what is needed to model the bulk phonons (80 meV), but in good agreement with calculated and measured surface phonons [33]. Hengsberger et al. [3] reported in an earlier paper the same type of measurement except that the sample temperature was 12 K. They reported a value of $\lambda = 1.18 \pm 0.07$, obviously quite different from the value obtained by LaShell et al. [4]. Undoubtedly, this discrepancy is due to the difficulties associated with determining the slope of the bands or $\mathrm{Re}\Sigma(\varepsilon_F)$ at the Fermi energy [4]. The problem is compounded by the fact that the photoemission spectra are cut off at the Fermi energy.

First-principles calculations of the EPC for holes in the surface state bands are now appearing in the literature, producing excellent agreement with experiment [7–9]. The most exciting feature of these calculations is that they furnish a microscopic picture of the spectral features in the Eliashberg function. Fig. 10 displays such a calculation for Be(0 0 0 1) [9]. The top panel is for a hole in the surface state band at the Fermi energy, and the bottom panel is for a hole at the SBZ center with a binding

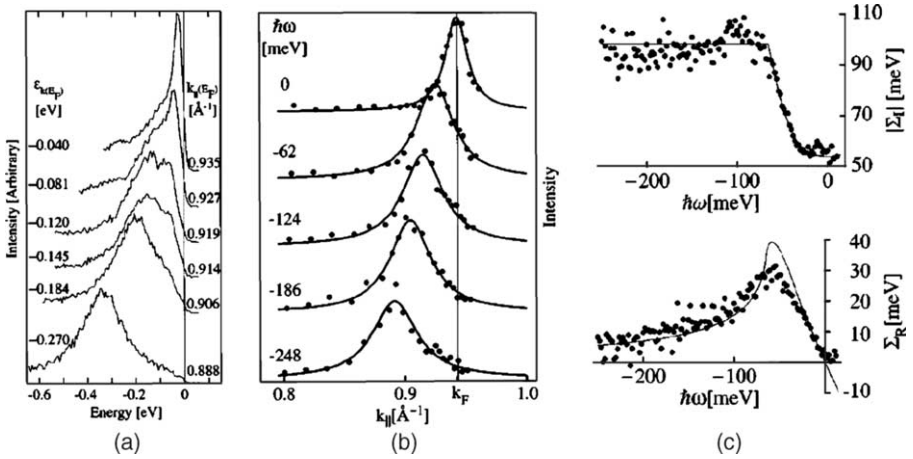

Fig. 9. High-resolution (energy 15 meV and momentum 0.008 Å^{-1}) angle-resolved photoemission data from the surface state on Be(0 0 0 1) at 40 K [4]. (a) Photoemission spectra at a fixed angle (k) showing intensity vs. energy. The distortion due to EPC near the Fermi energy is obvious. (b) A set of momentum distribution curves at fixed energy. (c) $\mathrm{Im}\Sigma(\varepsilon)$ at the top and $\mathrm{Re}\Sigma(\varepsilon)$ at the bottom. The solid curves are for a Debye model of the Eliashberg function [4]. The parameters are $\lambda = 0.65$ and $\omega_D = 65$ meV.

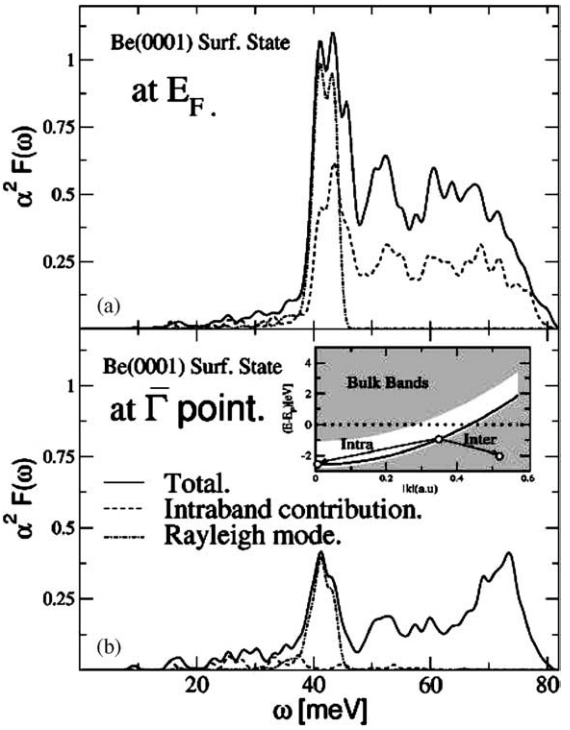

Fig. 10. Calculated Eliashberg functions for the surface state on Be(0 0 0 1) [9]. The top curve is for a hole at the Fermi energy, and the bottom curve is for a hole at the bottom of the surface state band [see Fig. 7(b)]. The inset shows the two different scattering mechanisms, intraband (surface state) and interband involving the bulk states. The different lines show the contribution to the Eliashberg function from intraband scattering (dashed line) and from Rayleigh mode scattering (dash-dotted line). The difference between the sum of these two curves and the total is due to interband scattering [9].

energy of 2.78 eV. Much new physics is contained in these curves. First and foremost, the Eliashberg function is different for a hole at the Fermi energy compared with a hole at the bottom of the band. When Eq. (9) is used to calculate the mass enhancement factor λ there is a dramatic dependence on the energy. At the Fermi energy, $\lambda(0) = 0.87$, while at the bottom of the band, $\lambda(-2.87\ \text{eV}) = 0.37$. As might have been expected $\lambda(\varepsilon)$ and as a consequence, it is not legitimate to measure $\lambda(\varepsilon)$ far from the Fermi energy and then conclude that the large mass enhancement might drive a physical phenomenon (like superconductivity) that depends on $\lambda(\varepsilon_F)$ [12]. It should be pointed out that Matzdorf et al. [11] in 1996 realized that mass enhancement factors far from the Fermi energy would not be the same as the traditionally defined λ In their paper on Cu(1 1 1), they called their mass enhancement factor b, so it would not be confused with a true value of λ determined at the Fermi energy.

The second message from these calculations is that the scattering or decay mode of a hole at the Fermi energy and at the bottom of the band is quite different. The

Table 1
Compilation of the experimental and theoretical values of the mass enhancement factor λ. QWS is for quantum well states in thin films

Surface	k point	Energy	Procedure	λ (surface)	λ (bulk)	Reference
Experiment						
Cu(1 1 1)	Γ	−0.42	$\mathrm{Im}\Sigma(T)$	0.14 ± 0.02	0.15	[10]
Cu(1 1 1)	Γ	−0.42	$\mathrm{Im}\Sigma(T)$	0.137 ± 0.015	0.15	[11]
Cu(1 1 1)	M	−2	$\mathrm{Im}\Sigma(T)$	0.085 ± 0.015	0.15	[11]
Cu(1 1 0)	Y	−0.51	$\mathrm{Im}\Sigma(T)$	0.23 ± 0.02	0.15	[13]
Cu(1 1 1)	Γ	−0.42	$\mathrm{Im}\Sigma(T)$	0.11	0.15	[7]
Ag(1 1 1)	Γ	−0.08	$\mathrm{Im}\Sigma(T)$	0.12	0.15	[7]
Be(0 0 0 1)	Γ	−2.78	$\mathrm{Im}\Sigma(T)$	1.15	0.24	[12]
Be(0 0 0 1)	k_F	0	$\mathrm{Re}\Sigma(\varepsilon)$	0.65	0.24	[4]
Be(0 0 0 1)	k_F	0	$\mathrm{Re}\Sigma(\varepsilon)$	1.18	0.24	[3]
Be(1 0 1 0)	$A[S_1]$	−0.37	$\mathrm{Im}\Sigma(T)$	0.65 ± 0.02	0.24	[17]
Be(1 0 1 0)	$A[S_2]$	−2.62	$\mathrm{Im}\Sigma(T)$	0.49 ± 0.4	0.24	[17]
Be(1 0 1 0)	$k(F)[S_1]$	0	$\mathrm{Re}\Sigma(\varepsilon)$	0.65 ± 0.02	0.24	[6]
Mo(1 1 0)	$\Gamma \rightarrow N$	0	$\mathrm{Im}\Sigma(T)$	0.42	0.24	[2]
V(0 0 1)	k_F	0	$\mathrm{Re}\Sigma(\varepsilon)$	1.45	−0.4	[14]
Bi(0 0 1)	$\Gamma \rightarrow k_2$		$\mathrm{Im}\Sigma(T)$	$0.02 \rightarrow 0.72$	−0.13	[18]
HAV(1 1 0)	$\Gamma \rightarrow S$	0	$\mathrm{Re}\Sigma(\varepsilon)$	1.4 ± 0.1	0.2	[5]
Ag/V(0 0 1)	Γ	QWSs	$\mathrm{Im}\Sigma(T)$	$0.2 \rightarrow 1.0$	0.15(Ag)	[14]
Ag/Fe(0 0 1)	Γ	QWSs	$\mathrm{Im}\Sigma(T)$	$\sim 0.3 \rightarrow \sim 1.0$	0.15(Ag)	[16]
Theory						
Cu(1 1 1)	Γ	−0.42		0.16	0.15	[7]
Ag(1 1 1)	Γ	−0.08		0.12	0.15	[7]
Al(1 0 0)	Γ	−2.7		0.23	0.44	[8]
Al(1 0 0)	k_F	0		0.56	0.44	[8]
Be(0 0 0 1)	Γ	−2.78		0.38	0.24	[9]
Be(0 0 0 1)	k_F	0		0.88	0.24	[9]

decay of a hole at the Fermi energy is dominated by the intraband scattering contribution (dashed line) and by the Rayleigh mode scattering (dash-dotted line). If the decay into the surface state at the $\overline{M}$ point of the SBZ is included, then 90% of the total (black line) is from surface processes. In contrast, the decay of a hole at the bottom of the band (lower panel) is radically different, being dominated by decay into bulk states (interband) [9].

For completeness, Table 1 shows a compilation of published data for EPC at surfaces and interfaces.

3. An exciting future for EPC at surfaces

Recent developments in this field hold significant promise for having surface states on metal surfaces become the playground for EPC physics. This promise is to produce textbook examples elucidating the origin and nature of EPC in reduced

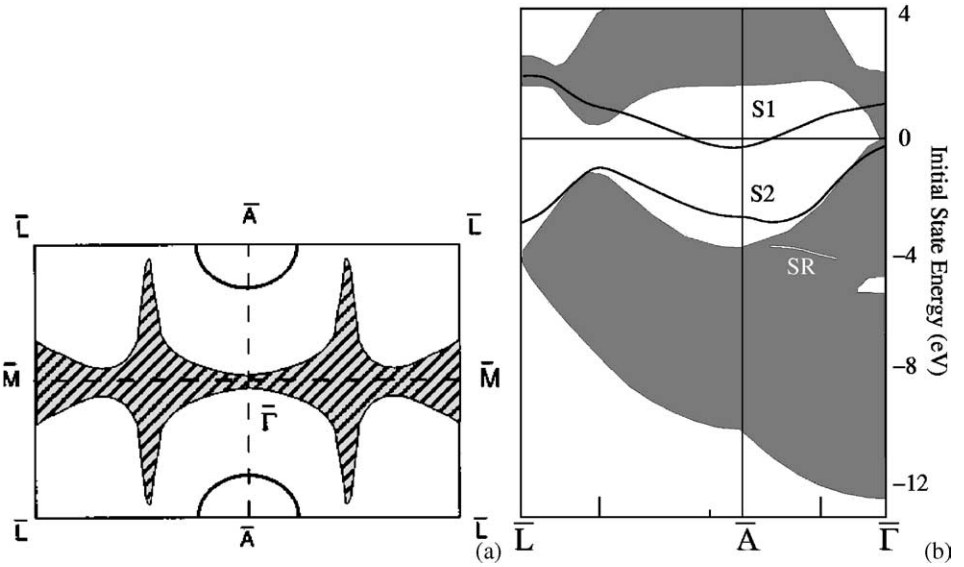

Fig. 11. Electronic properties of the Be(1 0 $\bar{1}$ 0) surface. (a) The projection of the bulk bands (shaded) onto the SBZ. The solid lines are the surface states [35,36]. (b) The projection of the bulk bands (shaded region) along the high-symmetry directions of the SBZ [37]. The calculated dispersion of the two surface states S_1 and S_2 is marked by the solid lines [37].

dimensionality and at the same time building a foundation for understanding EPC in more complex systems such at transition-metal oxides [34].

As the reader might have anticipated, the system that will be described is yet another surface of Be, Be(1 0 $\bar{1}$ 0) [6,17,35,36]. Fig. 11 shows the electronic properties of this surface in the same format as was used in Fig. 7 for Be(0 0 0 1). In panel (a), the projection of the bulk bands onto the SBZ at the Fermi energy is shown. The surface state of interest has a Fermi contour that is an elliptical shape about the SBZ point $\overline{A}$. Panel (b) shows the projection of the bulk bands and the surface states along two high-symmetry directions in the SBZ [17]. Temperature-dependent measurements of the photoemission linewidth by Tang et al. [17] revealed that the EPC of the two surface states in the same band gap were dramatically different. The data for the deep state S_2 with a binding energy of 2.62 eV could be fitted with a Debye model ($\omega_D = 60$ meV) resulting in a value of $\lambda(S_2) = 0.491 \pm 0.04$. But the data for the upper surface state S_1 with a binding energy of 0.37 eV could not be fitted using a Debye model for the Eliashberg function. The best fit was achieved using an Einstein model ($\omega_E = 64$ meV) with a significantly larger mass enhancement factor, $\lambda(S_1) = 0.646 \pm 0.02$. It was pointed out in this paper that there is a strong surface optical phonon at the SBZ boundary in both experiment and theory [38,39]. High-resolution angle-resolved photoemission measurements of the S_1 surface state band dispersion along the $\overline{\Gamma}$ to $\overline{A}$ direction in the SBZ show a large EPC distortion of the band. The data are shown in the inset of Fig. 12(a) [6]. From these data, the $\mathrm{Re}\Sigma(\varepsilon)$

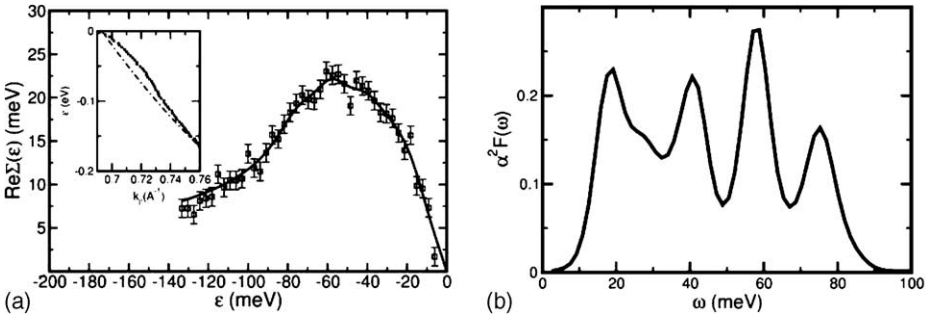

Fig. 12. (a) The $\mathrm{Re}\Sigma(\varepsilon)$ determined from the measured dispersion of the S_1 surface state in the $\overline{\Gamma}$ to $\overline{A}$ direction of the SBZ shown in Fig. 11(a) [6]. The inset shows the measured dispersion compared with the undistorted single-particle band dispersion. (b) The Eliashberg function extracted from the data shown in (a) using MEM [6]. The solid curve in (a) shows the fit to the original data.

was extracted and is presented in Fig. 12(a). Preliminary attempts to calculate the slope of $\mathrm{Re}\Sigma(\varepsilon)$ at the Fermi energy gave numbers of λ as large as 0.88.

The major advancement that will take this field and subject to new heights is the development by Shi et al. [6] of a technique for extracting the Eliashberg function from the high-resolution angle-resolved photoemission data. This extraction involves an integral inversion from Eq. (6), which was accomplished using the maximum entropy method (MEM) [6]. The MEM is a systematic way to incorporate the priori knowledge into a data fitting process. The priori knowledge inputted into the fitting procedure was (1) the Eliashberg function is positive, (2) there is a cutoff of the phonon density of states at some maximum energy ω_{M}, and (3) the low-energy phonon density of states has to look Debye-like [6]. The MEM procedure was shown to be robust against the imperfections in the data and the choice of the input fitting parameters. The fit to the $\mathrm{Re}\Sigma(\varepsilon)$ for Be(1 0 $\bar{1}$ 0) is shown in Fig. 12(a), and the Eliashberg function obtained using MEM to do the integral inversion is displayed in Fig. 12(b). There are three peaks at 40, 58, and 75 meV and a broad (double-humped) band which are undoubtedly due to the Rayleigh mode or modes around 20 meV. Fig. 13 shows a direct comparison of the experimental Eliashberg function for Be(1 0 $\bar{1}$ 0) with the first-principles calculation of the surface phonon dispersion in two of the high-symmetry directions of the SBZ [39]. The colored circles [1] in Fig. 13(a) are the modes localized at the surface. The correspondence between the calculated phonon modes and the Eliashberg function is quite amazing.

The red curve on Fig. 13(b) is the bulk phonon density of states [32]. Just as in the case of Be(0 0 0 1) (displayed in the upper panel of Fig. 10), a large fraction of the weight in the Eliashberg function comes from the surface Rayleigh modes. Eq. (9) shows that λ is defined as the first reciprocal moment of the Eliashberg function; consequently, the low-energy structure contributes more significantly to the mass

[1] For interpretation of colours in this figure, the reader is referred to the web version of this article.

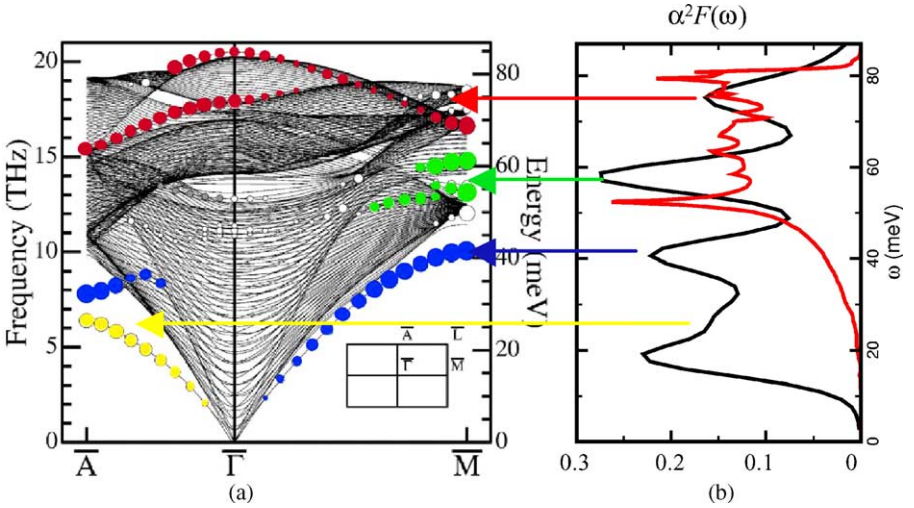

Fig. 13. A comparison of the calculated surface phonon dispersion along two high-symmetry directions for Be(1 0 $\bar{1}$ 0) [39] with the Eliashberg function extracted from the data shown in Fig. 12(a).

enhancement factor than the high-energy phonon structure. Using Eq. (9) and the Eliashberg function extracted from the data yields $\lambda(\varepsilon_F) = 0.65 \pm 0.06$. Three-fourths (75%) of this number comes from the two low-energy surface Rayleigh modes, raising a very interesting question. *Is the enhanced EPC seen for many metal surfaces a consequence of the ever present low-energy Rayleigh surface modes*?

Another general observation at this early stage of the study of EPC at metal surfaces is that a high density of surface states at the Fermi energy coupled with a low density of bulk states seems to be a common feature [15]. A comparison of the bulk density of states for Be and the surface density of states for Be(0 0 0 1) and Be(1 0 $\bar{1}$ 0) [30,35] is shown in Fig. 14. This is also the general picture for W(1 1 0) and Mo(1 1 0) [5,15]. It has been speculated that the 400 increase in the superconducting temperature for amorphous Be compared with crystalline Be is the result of an in-

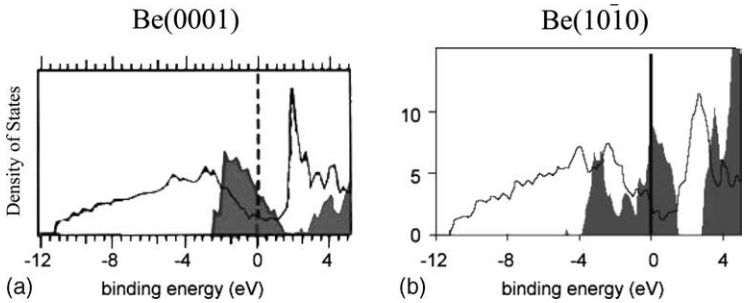

Fig. 14. The enhanced density of states at the Fermi energy due to the presence of surface states for Be(0 0 0 1) and Be(1 0 $\bar{1}$ 0) (shaded) compared with the bulk density of states [30,35].

crease in the density of states at the Fermi energy caused by interface states. *Is this a signature of enhanced EPC at metal surfaces*?

In conclusion, exciting times lie ahead. For the first time, the **k** dependence of the Eliashberg function can and will be measured. The surface community knows how to move surface states around in the band gap by adsorption of ordered or disordered arrays of atoms or molecules. As the surface states shift, there will also be a concomitant distortion in the surface phonon spectra, which can be measured and correlated with the structure in the Eliashberg function. Atoms such as H will produce dispersionless high-energy optical phonons that could lead to significant EPC [5,15]. When $\lambda >\sim 1$, the system should become unstable, either toward a reconstruction or some form of phonon-mediated pairing. Can the EPC be engineered at a surface to drive the creation of an instability [40]? Can we use these techniques to investigate couplings to magnetic excitations at a surface?

Acknowledgements

The work of EWP and S.-J. Tang was supported by NSF DMR 0105232. ALS is supported by DOE's Office of BES, Division of Materials Sciences and Engineering, under contract DE-AC03-76SF00098. Oak Ridge National Laboratory is managed by UT-Battelle, LLC, for the U.S. Department of Energy under Contract DE-AC05-00OR22725.

References

[1] G. Grimvall, in: E. Wohlfarth (Ed.), The Electron–Phonon Interaction in Metals, Selected Topics in Solid State Physics, North-Holland, New York, 1981.
[2] T. Valla, A.V. Fedorov, P.D. Johnson, S.L. Hulbert, Phys. Rev. Lett. 83 (1999) 2085.
[3] M. Hengsberger, D. Purdie, P. Segovia, M. Garnier, Y. Baer, Phys. Rev. Lett. 83 (1999) 592.
[4] S. LaShell, E. Jensen, T. Balasubramanian, Phys. Rev. B 61 (2000) 2371.
[5] E. Rotenberg, J. Schaefer, S.D. Kevan, Phys. Rev. Lett. 84 (2000) 2925.
[6] J. Shi, S.-J. Tang, B. Wu, P.T. Spunger, W.L. Yang, V. Broue, X.J. Zhou, X.X. Shen, Z. Zhang, E.W. Plummer, ArXiv:cond-mat/0308055v1.
[7] A. Eiguren, B. Hellsing, F. Reinert, G. Nicolay, E.V. Chulkov, V.M. Sinkin, S. Hüfner, P.M. Echenique, Phys. Rev. Lett. 88 (2002) 066805.
[8] A. Eiguren, B. Hellsing, E.V. Chulkov, P.M. Echenique, Phys. Rev. B 67 (2003) 235423.
[9] A. Eiguren, S. de Gironcoli, E.V. Chulkov, P.M. Echenique, E. Tosatti, in press.
[10] B.A. McDougall, T. Balasubramanian, E. Jensen, Phys. Rev. B 51 (1995) 13891.
[11] R. Matzdorf, G. Meister, A. Goldmann, Phys. Rev. B 54 (1996) 14807.
[12] T. Balasubramanian, E. Jensen, X.L. Wu, S.L. Hulbert, Phys. Rev. B 57 (1998) R6866.
[13] P. Straube, F. Pforte, T. Michalke, K. Berge, A. Gerlach, A. Goldmann, Phys. Rev. B 61 (2000) 14072.
[14] M. Kralj, A. Siber, P. Pervan, M. Milun, T. Valla, P.D. Johnson, D.P. Woodruff, Phys. Rev. B 64 (2001) 085411.
[15] S.D. Kevan, E. Rotenberg, J. Electron. Spectrosc. Relat. Phenom. 117–118 (2001) 57.
[16] D.-A. Luh, T. Miller, J.J. Paggel, T.-C. Chiang, Phys. Rev. Lett. 88 (2002) 256802.
[17] S.-J. Tang, Ismail, P.T. Sprunger, E.W. Plummer, Phys. Rev. B 65 (2000) 235428.

[18] J.E. Gayone, S.V. Hoffmann, Z. Li, Ph. Hofmann, submitted for publication.
[19] W. Kohn, Phys. Rev. Lett. 2 (1959) 545.
[20] R.H. Gaylord, K. Jeong, S.D. Kevan, Phys. Rev. Lett. 62 (1989) 2036.
[21] E. Hulpke, J. Lüdecke, Phys. Rev. Lett. 68 (1992) 2846;
E. Hulpke, J. Lüdecke, Surf. Sci. 272 (1992) 289.
[22] B. Kohler, P. Ruggerone, S. Wilke, M. Scheffler, Phys. Rev. Lett. 74 (1995) 1387;
B. Kohler, P. Ruggerone, M. Scheffler, Phys. Rev B 56 (1997) 13503.
[23] C. Bungaro, S. de Gironcoli, S. Baroni, Phys. Rev. Lett. 77 (1996) 2491.
[24] M. Balden, S. Lehwald, H. Ibach, Phys. Rev. B 53 (1996) 7479.
[25] G. Grüner, Density Waves in Solids, Addison-Wesley, Reading, MA, 1994.
[26] M. Hochstrasser, J.G. Tobin, E. Rotenberg, S.D. Kevan, Phys. Rev. Lett. 89 (2002) 216802.
[27] S. LaShell, B.A. McDougall, E. Jensen, Phys. Rev. Lett. 77 (1996) 3419.
[28] Y.J. Chabal, Phys. Rev. Lett. 55 (1985) 845.
[29] D.C. Langreth, Phys. Rev. Lett. 54 (1985) 126.
[30] E.V. Chulkov, V.M. Silkin, E.N. Shirykalov, Surf. Sci. 188 (1987) 287.
[31] R. Stumpf, J.B. Hannon, P.J. Feibelman, E.W. Plummer, in: E. Bertel, M. Donath (Eds.), Electronic Surface and Interface States on Metallic Systems, World Scientific, Singapore, 1995, p. 151.
[32] R. Bartynski, E. Jensen, T. Gustafsson, E.W. Plummer, Phys. Rev. B 32 (1985) 1921.
[33] J.B. Hannon, E.J. Mele, E.W. Plummer, Phys. Rev. B 53 (1996) 2090.
[34] Y. Tokura, Phys. Today 56 (2003) 50.
[35] V.M. Silkin, E.W. Chulkov, Phys. Solid State 37 (1995) 1540.
[36] Ph. Hofmann, B.G. Briner, M. Doering, H.-P. Rust, E.W. Plummer, A.M. Bradshaw, Phys. Rev. Lett. 79 (1997) 265.
[37] J.H. Cho, private communication.
[38] Ph. Hofmann, E.W. Plummer, Surf. Sci. 377–379 (1997) 330.
[39] M. Lazzeri, S. de Gironcoli, Surf. Sci. 454–456 (2000) 442.
[40] J. Shi, B. Wu, X.C. Xie, E.W. Plummer, Zhenyu Zhang, Phys. Rev. Lett., in press.